RSC Advances

PAPER

View Article Online
View Journal | View Issue

Cite this: *RSC Adv.*, 2019, **9**, 24280

Facile synthesis of few-layer MoS_2 in MgAl-LDH layers for enhanced visible-light photocatalytic activity

Guoyuan Zheng,[ab] Caihong Wu,[ab] Jilin Wang,*[ab] Shuyi Mo,[ab] Yanwu Wang,[c] Zhengguang Zou,[ab] Bing Zhou[ab] and Fei Long *[ab]

Received 22nd May 2019
Accepted 8th July 2019

DOI: 10.1039/c9ra03858b

rsc.li/rsc-advances

A new photocatalyst, few-layer MoS_2 grown in MgAl-LDH interlayers (MoS_2/MgAl-LDH), was prepared by a facile two-step hydrothermal synthesis. The structural and photocatalytic properties of the obtained material were characterized by several techniques including powder X-ray diffraction (XRD), Raman spectroscopy, field emission scanning electron microscopy (FESEM), high-resolution transmission electron microscopy (HRTEM), Fourier transform infrared spectroscopy (FTIR), X-ray photoelectron spectroscopy (XPS), photoluminescence spectroscopy (PL) and UV-vis absorption spectroscopy. The MoS_2/MgAl-LDH composite showed excellent photocatalytic performance for methyl orange (MO) degradation at low concentrations (50 mg L^{-1} and 100 mg L^{-1}). Furthermore, even for a MO solution concentration as high as 200 mg L^{-1}, this composite also presented high degradation efficiency (>84%) and mineralization efficiency (>73%) at 120 min. The results show that the MoS_2/MgAl-LDH composite has great potential for application in wastewater treatment.

1. Introduction

Groundwater contamination due to dyes is still a serious environmental pollution problem, mainly because of the high toxicity and widespread use of dyes.[1–4] Semiconductor photocatalytic degradation of organic pollutants in wastewater using inexhaustible and environmentally friendly solar energy has attracted much attention.[5,6] TiO_2 is a commercially available semiconductor photocatalyst.[21,24] However, it shows poor utilization of sunlight, due to the wide band gap of 3.2 eV which only absorbs sunlight with a wavelength of less than 420 nm. Therefore, researchers have been looking for other semiconductor photocatalysts as replacements for TiO_2.

As a typical graphene-like transition metal disulfide, MoS_2 is a potential photocatalyst.[7–9,25] Unlike other semiconductor materials, based on the quantum confinement effect, the band gap of MoS_2 increases with the number of layers. Moreover, bulk MoS_2 is an indirect bandgap semiconductor with a band gap of 1.2 eV, and single-layer MoS_2 is a direct bandgap semiconductor with a band gap of 1.9 eV.[10] It can be seen that single-layer or few-layer MoS_2 is a potential photocatalytic semiconductor material. In addition, there are many unsaturated bonds and more active sites due to the complex edge structure of two-dimensional (2D) MoS_2. Therefore, preparation of single-layer or few-layer MoS_2 is particularly important for application in photocatalysis. For example, like for the preparation of graphene, single and few-layer MoS_2 have been prepared using mechanical exfoliation, the so-called "Scotch Tape Method".[11] Obviously, the "Scotch Tape Method" is not a scalable process. Recently the Coleman group prepared a single-layer of MoS_2 by a surfactant-assisted sonication pioneering method.[12–15] However, even if a single-layer of MoS_2 is prepared, the surface defects will lead to a high photoelectron–hole pair recombination efficiency, thus affecting the photocatalytic performance of MoS_2. Therefore, how to prepare single or few-layers of MoS_2 and inhibit the recombination of photoelectron–hole pairs is a challenging subject.

Based on the above reasons, we designed a single or few-layer MoS_2-intercalated layered double hydroxide (MoS_2/MgAl-LDH) composite as a novel photocatalyst. Few-layer MoS_2 can be obtained by the "space-confining" effect of the LDH interlayer. On the one hand, 2D MoS_2 can contribute more active sites. On the other hand, LDHs have excellent performance as carriers for photocatalyst composites. For example, Šárka *et al.* prepared ZnCr–CO_3 LDHs and derived mixed oxides that exhibited excellent adsorption and photocatalytic properties for Orange II.[35] Wu *et al.* prepared Cu_2O/ZnAl calcined layered double hydroxide (Cu_2O/ZnAl-CLDH) photocatalysts with superior photocatalytic activity.[33] Here we prepared MoS_2/MgAl-LDH

[a]*College of Materials Science and Engineering, Guangxi Key Laboratory of Optical and Electronic Materials and Devices, Guilin University of Technology, Guilin 541004, China. E-mail: longf@glut.edu.cn; jilinwang@glut.edu.cn; Fax: +86 773 5896672; Tel: +86 773 5896700*

[b]*Guilin University of Technology, Collaborative Innovation Center for Exploration of Hidden Nonferrous Metal Deposits and Development of New Materials in Guangxi, Guilin 541004, China*

[c]*College of Environmental Science and Engineering, Guilin University of Technology, Guilin 541004, China*

composites by hydrothermal synthesis, evaluated the catalytic performance of the catalyst by degrading methyl orange organic dyes, and conducted in-depth research on the synergistic mechanism of MoS_2 and MgAl-LDH.

2. Experimental

2.1. Synthesis of various materials

All reagents were analytical grade and used without further purification. MoS_2/MgAl-LDH was prepared by a simple two-step hydrothermal process. First, MgAl-LDH with MoO_4^{2-} intercalated in the interlayer (MoO_4^{2-}/MgAl-LDH) was prepared by a hydrothermal method. During the synthesis process, $Mg(NO_3)_2 \cdot 6H_2O$ (4.615 g) and $Al(NO_3)_3 \cdot 9H_2O$ (3.376 g) with a M^{2+}/M^{3+} molar ratio of 2.0/1.0 were dissolved in 50 mL degassed distilled water to form solution A. Then, NaOH (2.516 g) was dissolved in 25 mL degassed distilled water to produce solution B. $Na_2MoO_4 \cdot 2H_2O$ (7.561 g) was dissolved in 25 mL degassed distilled water to form solution C. Solutions A and B were added dropwise to a reaction vessel containing solution C with vigorous, constant stirring at a constant pH of 10 and at 60 °C. After the addition, the resultant slurry was cooled to room temperature and aged for 10 h at 140 °C. MoO_4^{2-}/MgAl-LDH was washed several times with large amounts of deionized water and lyophilized in a vacuum freeze dryer.

Then, MoO_4^{2-}/MgAl-LDH (0.5 g) and thiourea (0.38 g) were added to 60 mL degassed distilled water and stirred. After stirring, the resultant slurry was subsequently aged for 24 h at 205 °C. MoS_2/MgAl-LDH was washed several times with a large amount of deionized water and lyophilized in a vacuum freeze drier.

For comparison, MgAl-LDH with CO_3^{2-} intercalated in the interlayer (MgAl-LDH) was also fabricated by the same procedure except that solutions A and B were mixed dropwise in a reaction vessel without solution C. Pure MoS_2 was also prepared by hydrothermal processing. $Na_2MoO_4 \cdot 2H_2O$ (0.3 g) and thiourea (0.8 g) were dissolved in 65 mL degassed distilled water. The clear solution was aged for 24 h at 205 °C. Then, MoS_2 was washed several times with deionized water and lyophilized.

2.2. Characterization

The samples were characterized using X-ray diffraction (XRD, X'Pert PRO MRD), Raman spectroscopy (DXR Raman microscope), field emission scanning electron microscopy (FESEM, S-4800), high-resolution transmission electron microscopy (HRTEM, JEM-2100F), FTIR spectroscopy (Thermo Nicolet NEXUS 670), nitrogen adsorption–desorption experiments for surface and porosity quantification (NOVA-1200e) and X-ray photoelectron spectroscopy (XPS, ESCALAB 250Xi). The photoluminescence spectra of the materials were obtained with a fluorescence spectrophotometer (FluoroMax-4). The electrical behavior test was carried out using a semiconductor characterization system (4200-SCS). The degradation efficiency was determined by the concentration of MO studied by the spectrophotometer (UV-3600, Shimadzu). The mineralization efficiency was measured by a Total Organic Carbon analyzer (multi N/C 3100).

2.3. Photocatalytic activity

The photocatalytic efficiency was measured by the degradation of methyl orange (MO) as a model contaminant. In general, 50 mg catalyst (1 g L^{-1}) was added to a 50 mL MO solution with a certain initial concentration (50, 100, 150 or 200 mg L^{-1}), and the pH of the solution was adjusted by 0.1 mol L^{-1} HNO_3 or 1 mol L^{-1} NaOH (pH = 3, 5, 7, 9 and 11). The mixture was stirred in the dark for 30 min to achieve adsorption/desorption equilibrium of MO with the catalyst. Then, the reaction system was exposed to light irradiation from a 500 W xenon lamp ($\lambda > 420$ nm) using a photochemical reaction apparatus (BL-GHX-V). During irradiation, 3 mL of the reaction solution was removed with a pipette at specific time intervals. The photocatalyst was removed from the solution *via* centrifugation. The MO concentration was measured by an ultraviolet-visible spectrophotometer at $\lambda = 464$ nm.

The degradation efficiency was calculated by the following formula:

$$\text{Degradation efficiency (\%)} = 100 \times (C_0 - C)/C_0 \quad (1)$$

where C_0 is the initial concentration of MO (mg L^{-1}) and C is the concentration of MO at another given irradiation time (mg L^{-1}). The mineralization efficiency was calculated by the following formula:

$$\text{Mineralization efficiency (\%)} = 100 \times (\text{TOC}_0 - \text{TOC})/\text{TOC}_0 \quad (2)$$

where TOC_0 is the initial total organic carbon of MO (mg L^{-1}) and TOC is the total organic carbon of MO at another given irradiation time (mg L^{-1}).

3. Results and discussion

3.1. Structural design of the composite

The design of the MoS_2/MgAl-LDH composite is shown in Scheme 1. First, MoO_4^{2-} ions were added to the precursor solution of MgAl hydrotalcite. Due to the exchangeability of anions in the MgAl-LDH layers, MoO_4^{2-}/MgAl-LDH was prepared by a hydrothermal method. Subsequently, MoO_4^{2-}/MgAl-LDH was vulcanized in a hydrothermal process in a mild liquid phase environment. In this process, thiourea not only acts as a source of sulfur, but also releases H_2S as a protective atmosphere. In addition, in the liquid phase, it can improve the uniformity of the reaction sites of MoO_4^{2-} as well as acting as a sulfur source, which is beneficial to form few-layer MoS_2 in the MgAl-LDH layers.

3.2. Structural characterization of the composite

Fig. 1a shows the XRD patterns of MgAl-LDH, MoO_4^{2-}/MgAl-LDH, MoS_2 and MoS_2/MgAl-LDH. The XRD pattern of MgAl-LDH has four diffraction peaks at 11.7°, 23.4°, 34.9° and 60.8°, which correspond to the (003), (006), (012) and (110) planes, respectively, of MgAl-LDH with the general formula

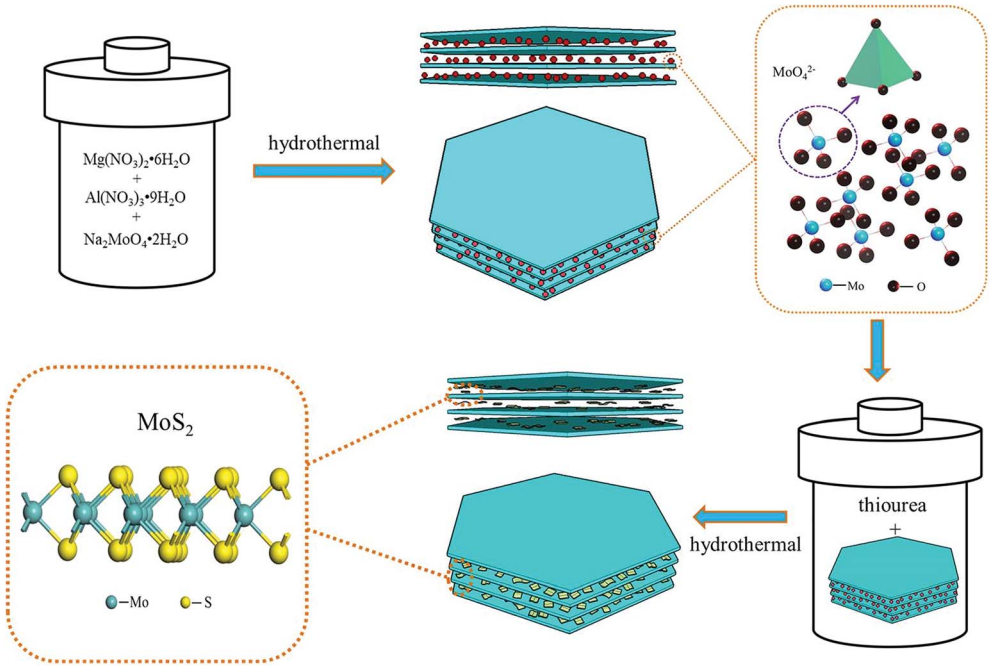

Scheme 1 Design of the MoS_2/MgAl-LDH growth process.

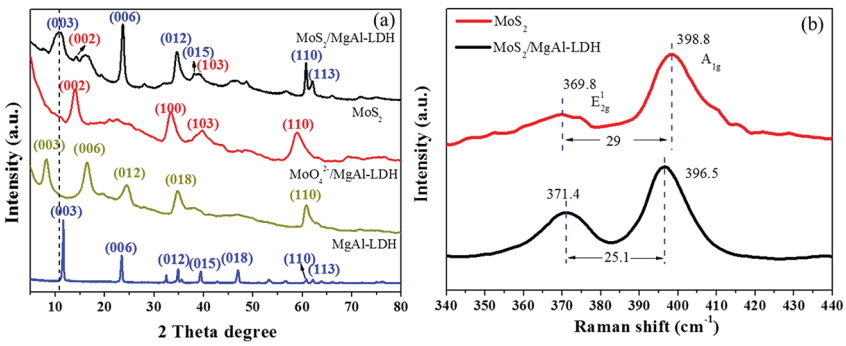

Fig. 1 XRD patterns of MgAl-LDH, MoO_4^{2-}/MgAl-LDH, MoS_2 and MoS_2/MgAl-LDH (a), and Raman spectra of MoS_2 and MoS_2/MgAl-LDH (b).

$(Mg_{0.667}Al_{0.333})(OH)_2(CO_3)_{0.167}(H_2O)_{0.5}$ (JPCDS no. 89-0460). The pristine MgAl-LDH pattern shows typical Bragg reflections of hexagonal LDH phases with interlayer carbonate anions. The MoO_4^{2-}/MgAl-LDH composite has major diffraction peaks at 8.2°, 16.5°, 24.7° and 60.8°, which correspond to the (003), (006), (012) and (110) planes, respectively, of MgAl-LDH. The MoS_2/MgAl-LDH composite not only has major diffraction peaks at 10.65°, 23.4°, 34.9° and 60.8°, corresponding to the (003), (006), (012) and (110) planes of MgAl-LDH, but also has major diffraction peaks at 14.1° and 39.5°, which can be attributed to the (002) and (103) planes of MoS_2, respectively. In addition, the "*a*" value of the unit cell parameter did not change (as shown in Table 1). The unit cell parameters of LDHs correspond to the cation–cation distance in the brucite layer, which can be calculated by $a = 2 \times d$ (110). When MoO_4^{2-} and MoS_2 were inserted into MgAl-LDH, the substrate spacing increased from 7.6 Å to 10.8 Å and 8.3 Å, respectively. As shown in Scheme 2, the length of the C–O bond in the CO_3^{2-} anion is 1.179 Å in MgAl-LDH. When MoO_4^{2-} replaced the CO_3^{2-} anion in the MgAl-LDH layer, the spacing of the (003) plane increased from 7.6 Å to 10.8 Å. This is because the length of the Mo–O bond in the MoO_4^{2-} anion is 1.787 Å, which is larger than that of the C–O bond in the CO_3^{2-} ion. When MoS_2 was inserted into the LDH interlayer, the spacing of the (003) plane decreased to 8.3 Å, even though the length of the Mo–S bond was 2.414 Å. This is attributed to the weakening of the hydrogen bonding force between the MoS_2 compounds and the LDH layer. Fig. 1b shows the Raman spectra, which further reveal the microstructure of MoS_2 and MoS_2/MgAl-LDH. For MoS_2, two different Raman peaks at 369.8 and 398.8 cm^{-1} are attributed to the typical E^1_{2g} and A_{1g} modes of hexagonal MoS_2 crystals, respectively. In the case of MoS_2/MgAl-LDH, the two MoS_2 peaks are shifted to 371.4 and 396.5 cm^{-1}. Obviously, the frequency difference between the E^1_{2g} and A_{1g} modes belonging to MoS_2 was 29 cm^{-1}, while for

Table 1 Structural characteristics of the samples obtained by hydrothermal synthesis[a]

	MgAl-LDH	MoO_4^{2-}/MgAl-LDH	MoS_2/MgAl-LDH	MoS_2
a (Å)	3.05	3.05	3.05	—
c (Å)	22.8	32.4	24.9	—
c' (Å)	7.6	10.8	8.3	—
The thickness of the interlayer gallery[b] (Å)	2.8	6.0	3.5	—
Band gap (eV)	—	—	1.82	1.61

[a] $a = 2d_{110}$, $c = 3d_{003}$ and $c = 3c'$. [b] The difference between c' and 4.8 Å (the thickness of the brucite-like sheet).[16]

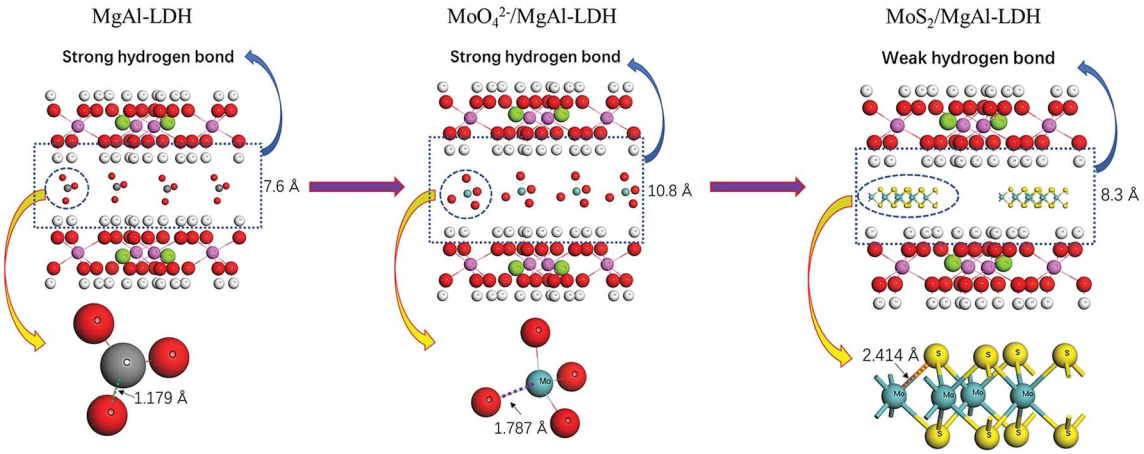

Scheme 2 Schematic of the spacing change of the (003) plane.

MoS_2/MgAl-LDH this was reduced to 25.1 cm^{-1}. This confirms that the thickness of the MoS_2 nanosheets has been significantly reduced.[36]

Fig. 2 shows the FTIR spectra of the various materials. As shown in Fig. 2a, strong and broad absorption bands at 3449, 3455 and 3449 cm^{-1} are observed for MgAl-LDH, MoO_4^{2-}/MgAl-LDH and MoS_2/MgAl-LDH, respectively. These can be attributed to the stretching vibration of the OH groups in the brucite-type layers and water molecules in the interlayer. The bands at 1618, 1635 and 1616 cm^{-1} can be attributed to the bending vibration of interlayer water. The absorption bands at 3422 and 1624 cm^{-1} for MoS_2 can be assigned to the stretching vibration of the OH groups and the bending vibrations of water molecules adsorbed on the MoS_2 surface, respectively. Between 1000 and 400 cm^{-1}, the bands can be assigned to metal–oxygen (M–O) and metal–hydroxyl (M–OH) vibrations.[17,18] The intense band characteristic of the ν_3 vibrations (antisymmetric stretching) of CO_3^{2-} ions located in the interlayer region can be observed at approximately 1360 cm^{-1}. The CO_3^{2-} peak intensities of MoS_2/MgAl-LDH and MoO_4^{2-}/MgAl-LDH are much weaker than those of MgAl-LDH in the FTIR spectra. For MoO_4^{2-}/MgAl-LDH, the antisymmetric stretching vibration band of Mo–O–Mo is observed at 820 cm^{-1}. The bands in the range of 400–1200 cm^{-1} for MoS_2 and MoS_2/MgAl-LDH are shown in Fig. 2b. In the

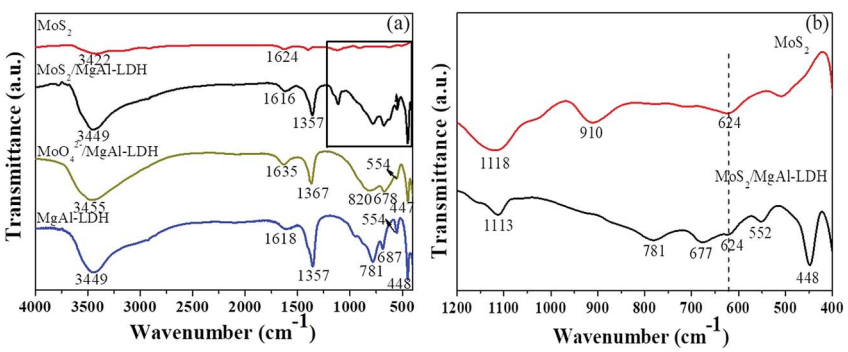

Fig. 2 FTIR spectra (a) of MgAl-LDH, MoS_2/MgAl-LDH and MoS_2 in the range of 400–4000 cm^{-1}; and (b) of MoS_2/MgAl-LDH and MoS_2 in the range of 400–1200 cm^{-1}.

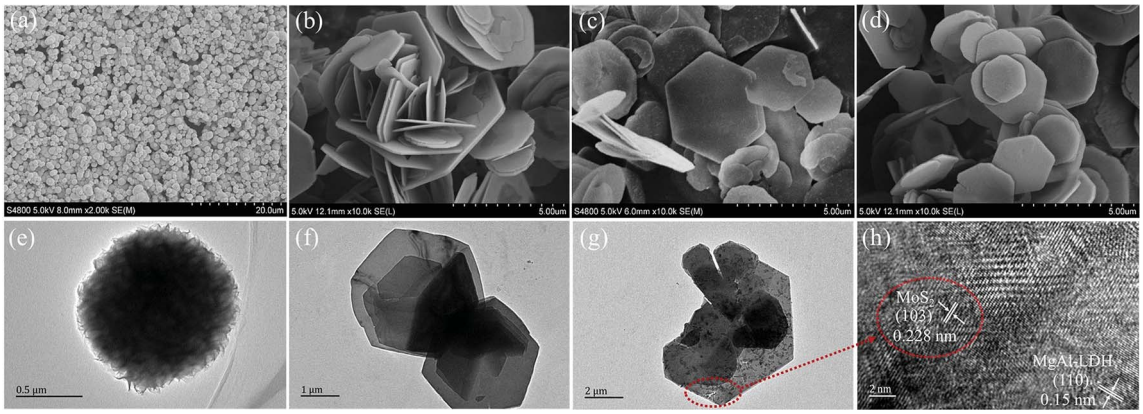

Fig. 3 FESEM images of MoS_2 (a), MgAl-LDH (b), MoO_4^{2-}/MgAl-LDH (c), and MoS_2/MgAl-LDH (d). TEM images of MoS_2 (e), MgAl-LDH (f), and MoS_2/MgAl-LDH (g) and HRTEM image of MgAl-LDH (h).

spectrum of MoS_2, the peak at 910 cm^{-1} can be attributed to the Mo═O stretching vibration, which may be caused by the formation of a small amount of oxide on the MoS_2 surface. The peaks at 1113 and 1118 cm^{-1} for MoS_2/MgAl-LDH and MoS_2, respectively, can be attributed to the S═O asymmetric stretching vibration. In the spectra of MoS_2/MgAl-LDH and MoS_2, the peak at 624 cm^{-1} can be assigned to the Mo–S stretching vibration.

Typical FESEM images of the samples are shown in Fig. 3a–d. As shown in Fig. 3a, the morphology of pure MoS_2 is flower-like. Moreover, each MoS_2 microsphere has an average diameter of approximately 1 μm. Fig. 3b–d show the morphology of MgAl-LDH, MoO_4^{2-}/MgAl-LDH and MoS_2/MgAl-LDH, respectively. It can be observed that all the samples maintain a hexagonal-like sheet structure. As shown in Fig. 3d, we didn't find any particles with a similar morphology to pure MoS_2 in the MoS_2/MgAl-LDH composite. This indicates that the morphology of MgAl-LDH has not changed after ion exchange and vulcanization. The microstructures of the samples were investigated through TEM (Fig. 3e–g) and HRTRM (Fig. 3h). Fig. 3e shows MoS_2 samples displaying flower-like spherical structures with diameters of 1–1.2 μm and Fig. 3f shows that MgAl-LDH is a highly dispersed flake. Interestingly, as shown in Fig. 3g, it is clearly shown that the MoS_2 nanosheet exhibits an irregular sheet-like structure in the layers of MgAl-LDH, and MgAl-LDH is decorated by MoS_2 and serves as a carrier. Moreover, the HRTEM image of MoS_2/MgAl-LDH is shown in Fig. 3h. The interplanar spacings of 0.228 and 0.15 nm can be attributed to the (103) and (110) planes of MoS_2 and MgAl-LDH, respectively. This also indicates that MoS_2 was successfully grown between the MgAl-LDH layers.

To verify the interfacial nature of MoS_2 and MgAl-LDH in the MoS_2/MgAl-LDH sample, XPS measurements were carried out. As shown in Fig. 4a, the XPS spectra of MoS_2/MgAl-LDH show Al 2p, S 2p, Mo 3d, C 1s, O 1s and Mg 1s binding energy peaks at 73.8 eV, 160.2 eV, 227.2 eV, 284.6 eV, 531.4 eV and 1303.7 eV, respectively. As shown in Fig. 4b, two peaks were observed at 228.3 and 231.6 eV, which could be attributed to Mo $3d_{5/2}$ and Mo $3d_{3/2}$ binding energies, respectively,[19,20] and are the characteristic peaks of Mo^{4+} in MoS_2. Two peaks at 232.5 and 235.7 eV are related to the Mo $3d_{5/2}$ and $3d_{3/2}$ binding energies of Mo^{6+}, respectively.[16] The small peak at 225.6 eV corresponds to the S 2s binding energy of MoS_2.[16] The S spectrum is shown in Fig. 4c. Two main peaks at 160.2 and 161.3 eV can be assigned to the S $2p_{3/2}$ and S $2p_{1/2}$ lines of MoS_2, respectively. The small peak at 167.5 eV suggests the existence of bridging disulfides S^{4+}.[22] As illustrated in Fig. 4d, the C 1s spectrum can be decomposed into a dominant peak at 284.6 eV for C═C/C–C[23] and a weak peak at 288.5 eV for C═O in oxygen-containing functional groups. The XPS results show that there is no chemical bond between MoS_2 and MgAl-LDH in the MoS_2/MgAl-LDH catalyst.

The XRD, FTIR, FESEM, HRTEM and XPS analysis showed that few-layer MoS_2 was successfully prepared in the MgAl-LDH layers by the hydrothermal method, which takes advantage of the "space-confining" effect of MgAl-LDH. Therefore, the synthetic design was reasonable *via* Scheme 1.

3.3. Photocatalytic performance

To better understand the photocatalytic performance of the MoS_2/MgAl-LDH composite, different solution pH values were used for the photodegradation of MO, as shown in Fig. 5a. The degradation rate of MoS_2/MgAl-LDH was the lowest at pH = 11, with only 19.23% of the MO degraded after 120 min. The photocatalytic ability of the sample increased as the pH decreased, and the degradation rate reached its highest at pH = 3, implying that the optimal photocatalytic capacity of MoS_2/MgAl-LDH occurred under acidic conditions. Fig. 5b compares the degradation rate and mineralization rate of MO under different pH values under visible light irradiation for 2 h. The degradation efficiency and mineralization efficiency of MO without the catalyst were only 0.48% and 0.09% respectively, which indicates that the MO molecule and intermediate products were difficult to self-degrade. When the MO solution pH = 3, the degradation efficiency and mineralization efficiency achieved 84.88% and 73.25%, respectively. Therefore, the optimal condition in this study was pH = 3.

The degradation rate using MoS_2/MgAl-LDH for different concentrations of MO is shown in Fig. 5c. The MO solution

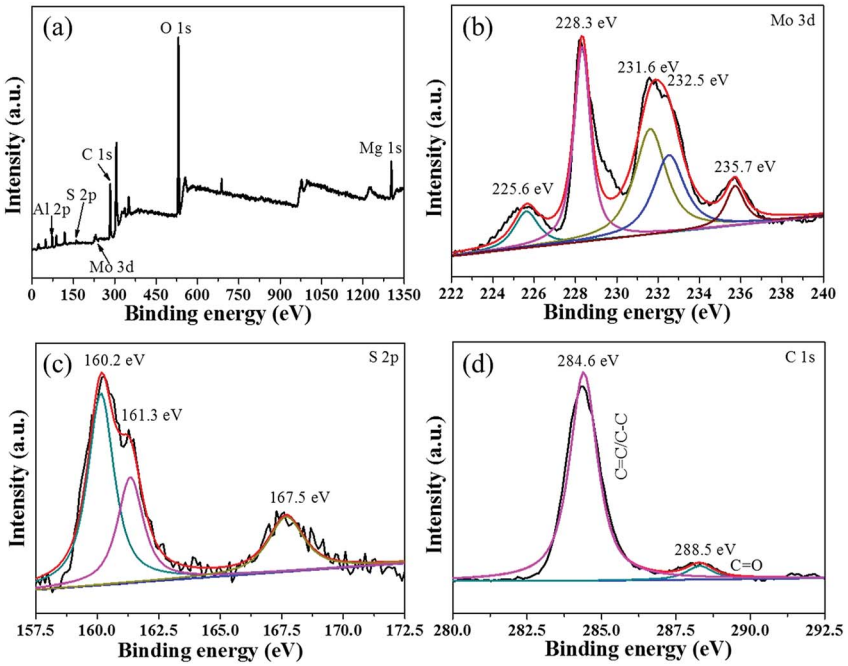

Fig. 4 XPS spectra of the MoS_2/MgAl-LDH sample (a) and high-resolution XPS spectra of Mo 3d (b), S 2p (c), and C 1s (d).

concentrations were 50, 100, 150 and 200 mg L^{-1}. As shown in Fig. 5c, the MO solutions with initial concentrations of 50 mg L^{-1} and 100 mg L^{-1} were completely degraded after reacting for 45 min and 105 min, respectively. In addition, the degradation efficiency was over 84% after 120 min when the initial concentrations of MO were 150 mg L^{-1} and 200 mg L^{-1}. In addition, the mineralization efficiency of MO (Fig. 5d) at initial concentrations of 50 mg L^{-1}, 100 mg L^{-1}, 150 mg L^{-1} and 200 mg L^{-1} achieved 97.25%, 96.74%, 79.56% and 73.25%, respectively. Compared with other catalysts (in Table 2), MoS_2/MgAl-LDH exhibited excellent catalytic performance at high concentrations of MO. To better verify the catalytic effect of the catalyst, a methyl orange concentration of 200 mg L^{-1} was selected for subsequent tests.

For comparison, pure MoS_2 and MgAl-LDH were also tested under the same conditions. The photocatalytic performances of the samples under visible-light irradiation are shown in Fig. 5e and f. The degradation efficiency and mineralization efficiency were 38.66% and 10.25% for MoS_2, 16.57% and 2.73% for MgAl-LDH, respectively. These are lower than the values (84.88% and 73.25%) for MoS_2/MgAl-LDH, indicating that the synergistic effect between MoS_2 and MgAl-LDH enhanced the catalytic activity.

Fig. 5g shows the MO kinetic analysis with MoS_2, MgAl-LDH and MoS_2/MgAl-LDH. The kinetics of photocatalytic reactions of organic pollutants are usually described by the Langmuir–Hinshelwood model. The photocatalytic process of MO can be expressed by the following pseudo first-order kinetic equation:[26]

$$-\ln\left(\frac{C_t}{C_0}\right) = K_{app}t \quad (3)$$

$$t_{1/2} = \frac{\ln 2}{K_{app}} \quad (4)$$

where C_0 and C_t are the initial MO concentration and the concentration at time t, respectively, and K_{app} is the photocatalytic reaction rate constant (min^{-1}). The K_{app}, linearization coefficient (R^2) and half-life ($t_{1/2}$) are given in Table 3. The high value of the linear regression coefficient (R^2) indicates that the photocatalytic reaction is well matched to the pseudo first-order kinetic model. MoS_2/MgAl-LDH showed the best photocatalytic performance, which was indicated by the largest value of K_{app}. The catalytic cycling performance of MoS_2/MgAl-LDH was investigated by reusing it four consecutive times as shown in Fig. 5h, and the degradation rate of MO was still above 80% after four cycles. This shows that the MoS_2/MgAl-LDH catalyst has excellent catalytic performance and reusability, even with a MO concentration as high as 200 mg L^{-1}. Fig. 5i shows the FTIR spectra of MoS_2/MgAl-LDH before and after photocatalysis. After photocatalysis, no characteristic peak of MO appeared in the FTIR spectra, proving that MoS_2/MgAl-LDH acts on MO *via* photocatalysis instead of adsorption.

3.4. The mechanism of the improvement in photocatalytic performance for MoS_2/MgAl-LDH

Fig. 6a and b show the nitrogen adsorption–desorption isotherms and corresponding BJH pore size distributions, respectively, of MoS_2, MgAl-LDH and MoS_2/MgAl-LDH. The isotherms are IV isotherms with H3 hysteresis loops, indicating porous flat agglomerates or lamellar particles.[37] The calculated BET surface area was 14.06 m^2 g^{-1} for MgAl-LDH, 13.18 m^2 g^{-1} for MoS_2, and 9.83 m^2 g^{-1} for MoS_2/MgAl-LDH. The results demonstrate that the excellent photocatalytic performance of

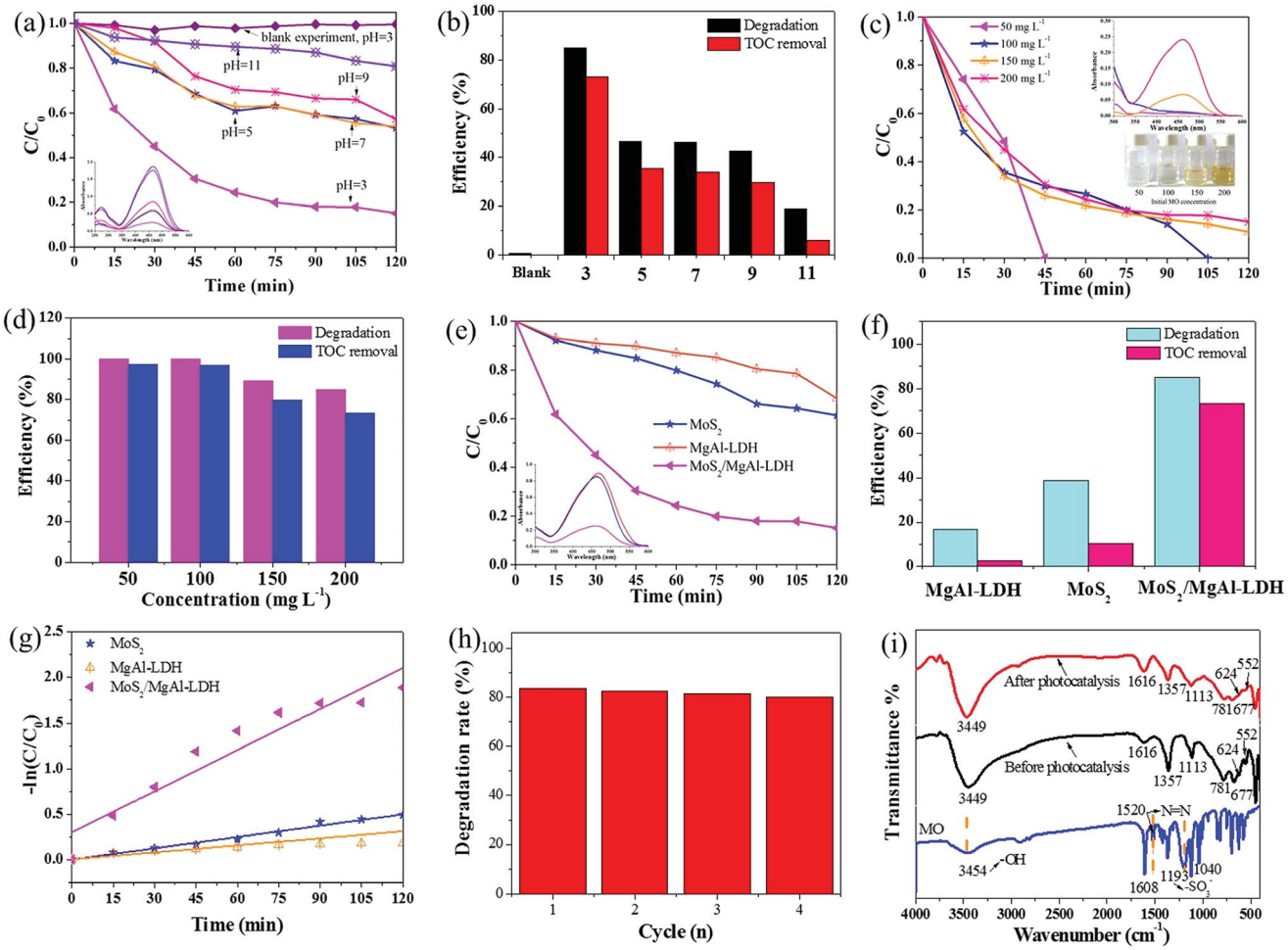

Fig. 5 Effect of initial solution pH values on the photodegradation (a) and mineralization (b) of MO (conditions: initial MO concentration 200 mg L^{-1}, photocatalyst dosage 1 g L^{-1}). Inset: UV-vis spectra of catalyzed solutions. Effect of initial MO concentration on the photodegradation (c) and mineralization (d) of MO (conditions: initial solution pH = 3, adsorbent dosage 1 g L^{-1}). Inset: the UV-vis spectra of catalyzed solutions (top) and optical photographs of supernatants obtained by centrifugation (bottom). Photocatalytic degradation curves (e) and mineralization efficiency (f) of the samples. Inset: the UV-vis spectra of catalyzed solutions. The kinetic analysis of the samples (g). Cycles of photocatalytic degradation of MO using MoS_2/MgAl-LDH (h) and FTIR spectra of MoS_2/MgAl-LDH before and after photocatalysis (i).

MoS_2/MgAl-LDH does not depend on the specific surface area. As shown in Fig. 6c, compared with that of pure MoS_2 and MgAl-LDH, the absorbance of MoS_2/MgAl-LDH in the visible region is enhanced. The enhanced absorption of MoS_2/MgAl-LDH will yield more photons to produce more photogenerated carriers, which could enhance the photocatalytic activity. The optical band gaps of the prepared photocatalysts were determined by the following equation ($\alpha = A(h\nu - E_g)^{n/2}/h\nu$).[38] As shown in Fig. 6d and e, the bandgap of MoS_2 increases from 1.62 to 1.78 eV, which is due to the decreasing domain size of MoS_2 grown in the MgAl-LDH layers. The recombination distance of electron–hole pairs is increased with the increased band gap of MoS_2.

Table 2 The photocatalytic activity of several photocatalysts for MO

Photocatalyst	MO concentration	Photocatalyst dosage	Results	References
TiO_2/MoS_2@zeolite	20 mg L^{-1}	0.5 g L^{-1}	Removal of 100% in 60 min	30
Ag/TiO_2	5×10^{-5} M (16.3 mg L^{-1})	1 g L^{-1}	Removal of 100% in 80 min	31
MoS_2/YVO_4	10 mg L^{-1}	1 g L^{-1}	Removal of 100% in 30 min	32
Cu_2O/ZnAl-CLDH	20 mg L^{-1}	1 g L^{-1}	Removal of approximately 90% in 420 min	33
TiO_2/biochar	20 mg L^{-1}	0.25 g L^{-1}	Removal of 100% in 150 min	34
MoS_2/MgAl-LDH	**50 mg L^{-1}**	**1 g L^{-1}**	**Removal of 100% in 45 min**	**This work**
	100 mg L^{-1}	**1 g L^{-1}**	**Removal of 100% in 105 min**	
	200 mg L^{-1}	**1 g L^{-1}**	**Removal of approximately 84% in 120 min**	

Table 3 Parameters of the pseudo first-order kinetic model for photocatalytic degradation

Photocatalysts	K_{app} (min^{-1})	R^2	$t_{1/2}$ (min)
MoS_2	0.00416	0.9832	166.59
MgAl-LDH	0.00259	0.89659	267.62
MoS_2/MgAl-LDH	0.01505	0.90051	46.06

To verify the synergistic mechanism between MoS_2 and MgAl-LDH in MoS_2/MgAl-LDH, photoluminescence (PL) measurements of the samples were also carried out. The PL spectra of the samples in the range λ = 265–330 nm with an excitation wavelength of 250 nm are shown in Fig. 6f. These materials exhibited a strong PL emission peak at $\lambda \approx 290$ nm due to charge carrier capture on the surface.[27] Compared with that of pure MoS_2 and MgAl-LDH, the PL signal of MoS_2/MgAl-LDH was the weakest, which indicated the sample had the lowest photogenerated electron–hole pair recombination rate[28] and the highest electron–hole pair separation efficiency. Obviously, the recombination efficiency of electron–hole pairs was inhibited in MgAl-LDH when MoS_2 grew in the MgAl-LDH layers.

Usually, nano-sized noble metals are used to modify the surfaces of semiconductors to form metal–semiconductor junctions to enhance electron–hole separation.[39] However, there is no metal–semiconductor junction found in MoS_2/MgAl-LDH composites, which can be confirmed by the above XPS results. Semiconductor testing is used to investigate the electrical behavior of the sample, as shown in Fig. 7. The samples were prepared into wafers 10 mm in diameter and 0.2 mm in thickness. Fig. 7a–c show the resistance tests of MgAl-LDH (Fig. 7a), MoS_2 (Fig. 7b) and MoS_2/MgAl-LDH (Fig. 7c), respectively. It can be clearly observed that the resistance meter of MgAl-LDH showed "O.L", indicating that the sample was nonconducting. Interestingly, the resistance of MoS_2 varied from 1.52 to "O.L", and the resistance of MoS_2/MgAl-LDH varied from 8.74 to "O.L". To better analyze the semiconductor characteristics of MoS_2 and MoS_2/MgAl-LDH, the samples were tested using a semiconductor characteristic system. Fig. 7d and e showed obvious semiconductor characteristic curves, indicating similar semiconductor properties between MoS_2/MgAl-LDH and MoS_2. It was likely that MgAl-LDH played the role of conductive layer in MoS_2/MgAl-LDH.

In addition, the effect of different capture agents on the photocatalytic activity of MoS_2/MgAl-LDH is shown in Fig. 8. The scavengers of O_2^-, h^+ and $OH^\bullet$ were benzoquinone (BQ), ethylenediaminetetraacetic acid (Na_2–EDTA) and isopropanol (IPA), respectively. It is shown that adding IPA significantly inhibited MO degradation, indicating that $OH^\bullet$ was one of the important active species in the photodegradation process. Likewise, the degradation ability of the composite is inhibited with the addition of Na_2–EDTA and BQ. Therefore, h^+ and $O_2^{-\bullet}$ are also major active species. In summary, $OH^\bullet$, h^+ and $O_2^{-\bullet}$ are the major active species for catalyzing MO in MoS_2/MgAl-LDH.

Based on the above discussion, the mechanism of the improvement in photocatalytic performance of MoS_2/MgAl-LDH is revealed in Scheme 3. On the one hand, few-layer MoS_2 nanosheets were prepared by the "space-confining" effect of MgAl-LDH. The bandgap of MoS_2 is increased from

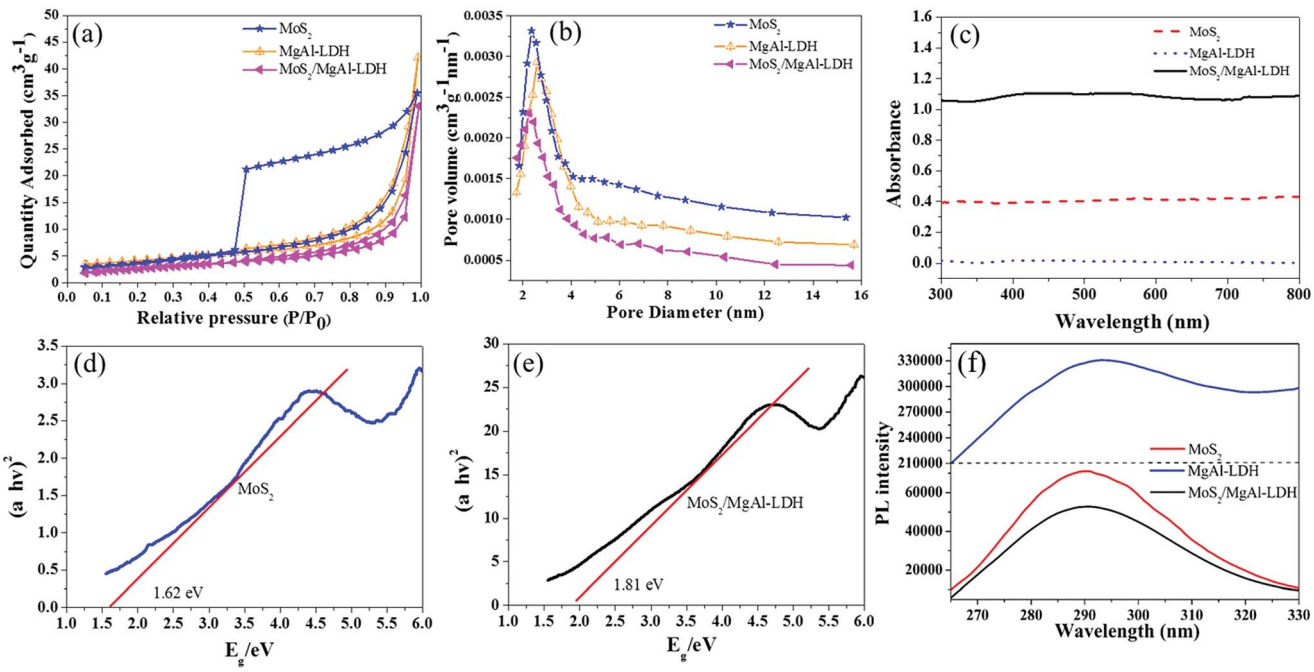

Fig. 6 N_2 adsorption–desorption isotherm curves (a) and pore size distribution curves (b) of the samples. UV-vis spectra of MgAl-LDH, MoS_2 and MoS_2/MgAl-LDH (c) and the bandgap curves of MoS_2 (d) and MoS_2/MgAl-LDH (e). Fluorescence spectra of MgAl-LDH, MoS_2 and MoS_2/MgAl-LDH (f).

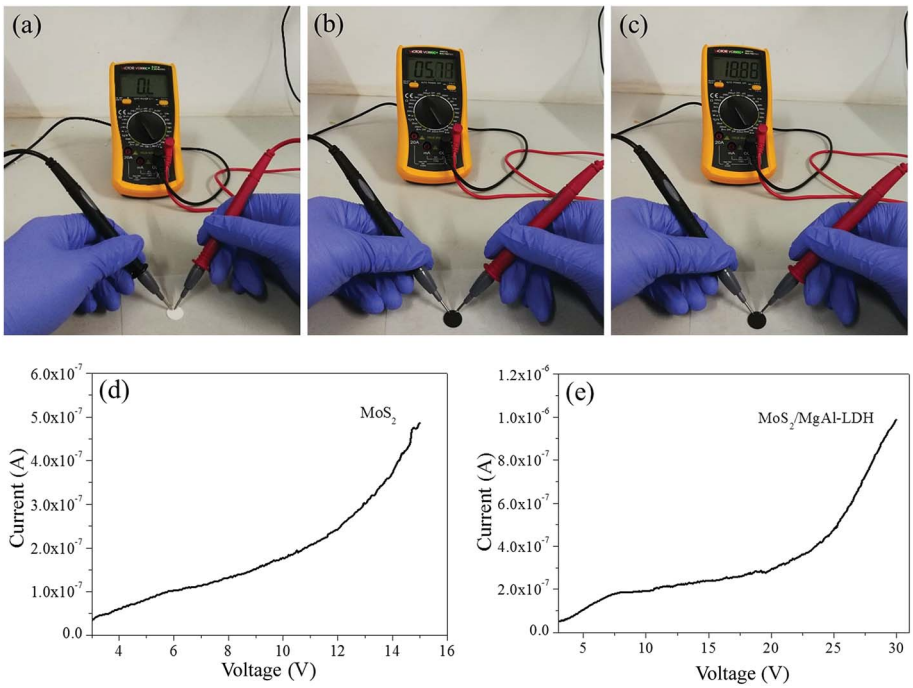

Fig. 7 Electrical characteristics of MgAl-LDH (a), MoS_2 (b), and MoS_2/MgAl-LDH (c). Semiconductor characteristic curves of MoS_2 (d), and MoS_2/MgAl-LDH (e).

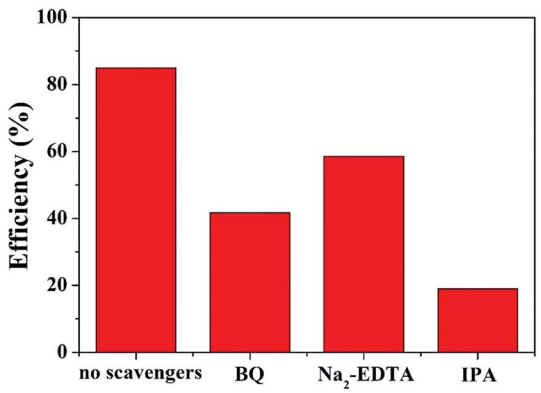

Fig. 8 Photocatalysis tests with different quenchers over MoS_2/MgAl-LDH.

1.62 to 1.81 eV due to the quantum limitation effect, leading the photogenerated electron–hole pairs having a stronger redox ability. On the other hand, the MgAl-LDH layer acts as an inorganic conductive layer, which could rapidly transfer photogenerated electrons from MoS_2, thus inhibiting the recombination of photogenerated electron–hole pairs. Moreover, a possible photocatalytic degradation mechanism can be proposed. First, the MO molecules are adsorbed in a layer on MoS_2/MgAl-LDH due to the charge on the surface of MgAl-LDH. Meanwhile, under visible light, photoelectrons and holes are generated in the conduction and valence bands, respectively, of MoS_2. Then, the photogenerated electrons transferred to the MgAl-LDH layer react with oxygen adsorbed on the surface or dissolved in water to produce superoxide. The excess holes on the valence band remain in MoS_2 and react with H_2O and OH^-

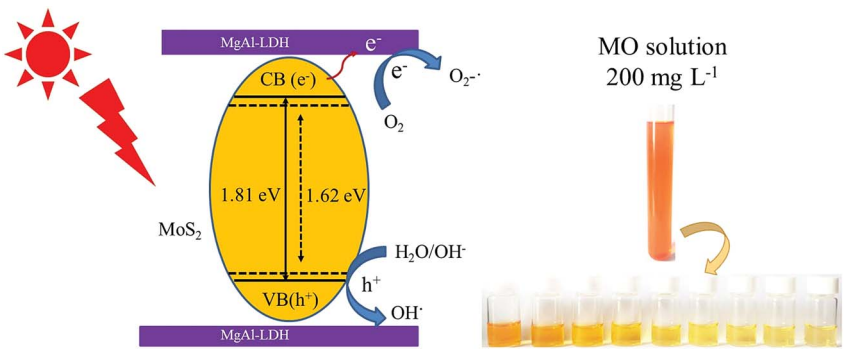

Scheme 3 Photocatalytic mechanism schematic of MO degradation by MoS_2/MgAl-LDH.

to form active substances such as $OH^{\bullet}$.[29] Then, photocatalysis proceeds by a known mechanism of visible-light-driven electron emission from the valence band to the conduction band, and the formation of oxidative intermediate species, $O_2^{-\bullet}$ and $^{\bullet}OH$, results in the degradation of MO.

$$MoS_2 + h\nu \rightarrow MoS_2(e^- + h^+) \quad (5)$$

$$MoS_2(e^-) + H^+ \rightarrow MoS_2 + H^{\bullet} \quad (6)$$

$$MoS_2(e^-) + O_2 \rightarrow MoS_2 + O_2^{-\bullet} \quad (7)$$

$$MoS_2(h^+) + OH^- \rightarrow OH^{\bullet} \quad (8)$$

$$MoS_2(h^+) + H_2O \rightarrow MoS_2 + H^+ + OH^{\bullet} \quad (9)$$

$$O_2^{-\cdot} + H^+ \rightarrow HO_2^{\cdot} \quad (10)$$

$$\text{Dye} + HO_2^{\cdot} \rightarrow \text{degradation products} \quad (11)$$

$$\text{Dye} + h^+ \rightarrow \text{oxidation products} \quad (12)$$

$$\text{Dye} + e^- \rightarrow \text{reduction products} \quad (13)$$

4. Conclusions

In summary, few-layer MoS_2 was successfully grown in MgAl-LDH layers. By decreasing the domain size of MoS_2, the bandgap of MoS_2 was increased from 1.62 eV (flower-like MoS_2) to 1.81 eV (MoS_2/MgAl-LDH), and the MoS_2/MgAl-LDH composite exhibits a significantly enhanced full-spectrum response in the wavelength range of 300–800 nm. More importantly, the MgAl-LDH layer acts as an inorganic conductive layer to transport photogenerated electrons efficiently. As a result, there is a lower recombination efficiency of photogenerated electron–hole pairs in the MoS_2/MgAl-LDH composite. Therefore, the MoS_2/MgAl-LDH composite exhibited an outstanding catalytic capacity and a superior cycle performance. The composite completely degraded the MO in 50 mg L^{-1} and 100 mg L^{-1} MO solutions in 45 min and 105 min, respectively. Furthermore, the composite also shows a degradation rate over 84% in 120 min even for a MO solution concentration as high as 200 mg L^{-1}, and retained 80% of the initial degradation rate after four cycles. The MoS_2/MgAl-LDH composite can be considered as a promising photocatalyst for waste water treatment.

Conflicts of interest

There are no conflicts to declare.

Acknowledgements

We acknowledge the financial support from the National Natural Science Foundation of China (No. 51672052), Guangxi Distinguished Experts Special Fund (2015B017), Guangxi Graduate Education Innovation Program and Improving the Basic Ability of Young and Middle-aged University Teachers in Guangxi (No. KY2018KY0256).

References

1 K. Iqbal, A. Iqbal, A. M. Kirillov, B. Wang, W. Liu and Y. Tang, *J. Mater. Chem. A*, 2017, **5**, 6716–6724.
2 J. S. Valentea, F. Tzompantzib and J. Princec, *Appl. Catal., B*, 2011, **102**, 276–285.
3 X. Liu, X. Zhao, Y. Zhu and F. Zhang, *Appl. Catal., B*, 2013, **140**, 241–248.
4 V. K. Gupta and T. A. Saleh, *Environ. Sci. Pollut. Res. Int.*, 2013, **20**, 2828–2843.
5 O. Legrini, E. Oliveros and A. M. Braun, *Chem. Rev.*, 1993, **93**, 671–698.
6 H. Li, J. Li, C. Xu, P. Yang, D. H. L. Ng, P. Song and M. Zuo, *J. Alloys Compd.*, 2017, **698**, 852–862.
7 J. Cha, K. Koski, K. Huang, K. Wang, W. Luo and D. Kong, *Nano Lett.*, 2013, **13**, 5913–5918.
8 K. Wang, J. Wang, J. Fan, M. Lotya, A. O'Neill, D. Fox, Y. Feng, X. Zhang, B. Jiang, Q. Zhao, H. Zhao, J. Coleman, L. Zhang and W. Blau, *ACS Nano*, 2013, **7**, 9260–9267.
9 Y. Li, Y. Rao, K. F. Mak, Y. You, S. Wang, C. R. Dean and T. F. Heinz, *Nano Lett.*, 2013, **13**, 3329–3333.
10 T. Li and G. Galli, *J. Phys. Chem. C*, 2007, **111**, 16192–16196.
11 A. Splendiani, L. Sun, Y. Zhang, T. Li, J. Kim, C. Y. Chim, G. Galli and F. Wang, *Nano Lett.*, 2010, **10**, 1271–1275.
12 M. Lotya, Y. Hernandez, P. J. King, R. J. Smith, V. Nicolosi, L. S. Karlsson, F. M. Blighe, S. De, Z. Wang, I. T. McGovern, G. S. Duesberg and J. N. Coleman, *J. Am. Chem. Soc.*, 2009, **131**, 3611–3620.
13 M. Lotya, P. J. King, U. Khan, S. De and J. N. Coleman, *ACS Nano*, 2010, **4**, 3155–3162.
14 R. J. Smith, P. J. King, M. Lotya, C. Wirtz, U. Khan, S. De, A. O'Neill, G. S. Duesberg, J. C. Grunlan, G. Moriarty, J. Chen, J. Wang, A. I. Minett, V. Nicolosi and J. N. Coleman, *Adv. Mater.*, 2011, **23**, 3944–3948.
15 M. D. J. Quinn, N. H. Ho and S. M. Notley, *ACS Appl. Mater. Interfaces*, 2013, **5**, 12751–12756.
16 M. Li, L. Zhang, X. Fan, M. Wu, Y. Du, M. Wang, Q. Kong, L. Zhang and J. Shi, *Appl. Catal., B*, 2016, **190**, 36–43.
17 S. Mancipe, F. Tzompantzi and R. Gómez, *Appl. Clay Sci.*, 2017, **136**, 67–74.
18 P. Kuśtrowski, A. Rafalska-Łasocha, D. Majda, D. Tomaszewska and R. Dziembaj, *Solid State Ionics*, 2001, **141**, 237–242.
19 Y. Shi, Y. Wang, J. I. Wong, A. Y. S. Tan, C. L. Hsu, L. J. Li, Y. C. Lu and H. Y. Yang, *Sci. Rep.*, 2013, **3**, 2169.
20 Y. Sun, X. Hu, W. Luo and Y. Huang, *J. Mater. Chem.*, 2011, **22**, 425–431.
21 Y. Zhang, N. Afzal, L. Pan, X. Zhang and J. Zou, *Adv. Sci.*, 2019, **6**, 1900053–1900072.
22 V. O. Koroteev, L. G. Bulusheva, I. P. Asanov, E. V. Shlyakhova, D. V. Vyalikh and A. V. Okotrub, *J. Phys. Chem. C*, 2011, **115**, 21199–21204.

23 Y. Teng, H. Zhao, Z. Zhang, Z. Li, Q. Xia, Y. Zhang, L. Zhao, X. Du, Z. Du and P. Lv, *ACS Nano*, 2016, **10**, 8526–8535.
24 G. Shen, L. Pan, Z. Lü, C. Wang, F. Aleem, X. Zhang and J. Zou, *Chin. J. Catal.*, 2018, **39**, 920–928.
25 Z. Lv, N. Mahmood, M. Tahir, L. Pan, X. Zhang and J. Zou, *Nanoscale*, 2016, **8**, 18250–18269.
26 Y. Zhou, L. Shuai, X. Jiang, F. Jiao and J. Yu, *Adv. Powder Technol.*, 2015, **26**, 439–447.
27 C. Y. Lin, Y. C. Wang, S. J. Hsu, C. F. Lo and W. G. Diau, *J. Phys. Chem. C*, 2010, **114**, 176–184.
28 X. Liu, L. Pan, Q. Zhao, T. Lv, G. Zhu, T. Chen, T. Lu, Z. Sun and C. Sun, *Chem. Eng. J.*, 2012, **183**, 238–243.
29 M. O. Ansari, M. M. Khan, S. A. Ansari, I. Amal, J. Lee and M. H. Cho, *Mater. Lett.*, 2014, **114**, 159–162.
30 W. Zhang, X. Xiao, L. Zheng and C. Wan, *Appl. Surf. Sci.*, 2015, **358**, 468–478.
31 R. Saravanan, D. Manoj, J. Qin, M. Naushad, F. Gracia, A. F. Lee, M. M. Khan and M. A. G. Pinilla, *Process Saf. Environ. Prot.*, 2018, **120**, 339–347.
32 Q. Chen, C. Zhao, Y. Wang, Y. Chen, Y. Ma, Z. Chen, J. Yu, Y. Wu and Y. He, *Sol. Energy*, 2018, **171**, 426–434.
33 X. Wu, D. Zhang, F. Jiao and S. Wang, *Colloids Surf., A*, 2016, **508**, 110–116.
34 L. Lu, R. Shan, Y. Shi, S. Wang and H. Yuan, *Chemosphere*, 2019, **222**, 391–398.
35 P. Šárka, J. Krýsa, J. Jirkovský, F. Claude, M. Gilles and P. Vanessa, *Appl. Catal., B*, 2015, **170–171**, 25–33.
36 C. Lee, H. Yan, L. E. Brus, T. F. Heinz, J. Hone and S. Ryu, *ACS Nano*, 2010, **4**, 2695–2700.
37 S. Mancipe, F. Tzompantzi and R. Gómez, *React. Kinet., Mech. Catal.*, 2017, **122**, 625–634.
38 D. S. Ginley and M. A. Butler, *J. Appl. Phys.*, 1977, **48**, 2019–2021.
39 C. Liu, D. Kong, P. C. Hsu, H. Yuan, H. W. Lee, Y. Liu, H. Wang, S. Wang, K. Yan, D. Lin, P. A. Maraccini, K. M. Parker, A. B. Boehm and Y. Cui, *Nat. Nanotechnol.*, 2016, **11**, 1098–1104.